A three-dimensional micromechanically based model

Hao Xiong, François Nicot, Zhen-Yu Yin

A three-dimensional micromechanically based model

H. Xiong[1,*,†], F.Nicot[1] and Z. Y. Yin[2,3]

[1]*Université Grenoble Alpes, IRSTEA, Geomechanics Group, ETNA, Grenoble, France*
[2]*LUNAM University, Ecole Centrale de Nantes, UMR CNRS GeM, Nantes, France*
[3]*Key Laboratory of Geotechnical and Underground Engineering of Ministry of Education; Department of Geotechnical Engineering, College of Civil Engineering, Tongji University, Shanghai 200092, China*

Granular materials react with complicated mechanical responses when subjected to external loading paths. This leads to sophisticated constitutive formulations requiring large numbers of parameters. A powerful and straightforward way consists in developing micro-mechanical models embedding both micro-scale and meso-scale. This paper proposes a 3D micro-mechanical model taking into account an intermediate scale (meso-scale) that makes it possible to describe a variety of constitutive features in a natural way. The comparison between experimental tests and numerical simulations reveals the predictive capability of this model. Particularly, several simulations are carried out with different confining pressures and initial void ratios, based on the fact that the critical state is quantitatively described without requiring any critical state formulations and parameter. The model mechanism is also analyzed from a microscopic view, wherein the evolution of some key microscopic parameters is investigated.

granular materials; multiscale approach; microstructure; mesoscopic scale; micromechanics; critical state

1. INTRODUCTION

Granular materials are significant constituents involved in many industrial processes and geophysical phenomena. However, no fundamental statistical theory is currently available to describe their properties. The behavior of one single grain is easily understood, but the properties of a granular collection are much more complex. As such, considerable attempts have been made over last few decades to understand the behavior of granular materials, especially in soil mechanics. For the macroscopic aspect, several focal topics are wildly discussed such as strain localization [1], instability occurrence [2], and the existence of a bifurcation domain within the plastic limit surface, in which a variety of failure modes can be encountered [3–6]. These macroscopic features not only need to be observed but also need to be understood. Thus, increasing researches on the micro-scale are conducted to explain the physical background, including the particle breakage [7], the anisotropy [8, 9], the liquefaction [10, 11], the failure occurrence [2, 12], the force chain buckling [13], and the meso-structure evolution [14].

A variety of phenomenological models have been developed to describe complicated phenomena in soil mechanics. These models constantly involve enriched and complex mathematical equations introducing a great number of parameters to describe different observed phenomena. Some typical phenomenological models are reviewed here such as elastoplastic theories [15–19], endochronic models [20], hypoplastic theories [21], and incrementally nonlinear models [22, 23]. On the other

*Correspondence to: H. Xiong, Université Grenoble Alpes, IRSTEA, Geomechanics Group, ETNA, Grenoble, France.
†E-mail: xionghao19529@gmail.com

side, an increasing sight can be found in microscopic modeling and multiscale approaches on both numerical and experimental sides, with the development of microscopy technology and X-ray tomography [24]. It is an alternative way to consider that the variety of constitutive properties stem essentially from the granular character [25–27]. A series of micro-mechanical models have been proposed by considering the average behavior of all contacts along each contact direction [28, 29], or considering a meso-structure oriented along all the directions of the physical space [30].

In this paper, the micro-directional model [28] and the H-directional model [30] in 2D conditions are firstly reviewed. Based on the homogenization scheme of the H-directional model, a 3D extension of the H-directional model is developed. To examine the novel model capability, calibration is performed using drained triaxial experimental results from Ticino sand. Once calibrated, the performance of this 3D-H model is then analyzed in prediction. Afterwards, the model responses on confining stress-dependent and void ratio-dependent stress–strain relationships are examined, based on which the critical state seems naturally captured. Finally, the model mechanism is also inspected from a microscopic point of view. The evolution of micro variables is analyzed at different strain states along a drained triaxial loading path.

2. A BRIEF REVIEW OF THE TWO-DIMENSIONAL MICRO-DIRECTIONAL MODELS

These 2D models that consist of the micro-directional model [28] and the H micro-directional model [30] were initially developed to describe the mechanical behavior of snow [31]. The micro-directional model was then generalized to any type of granular assembly, with a particular emphasis on frictional granular materials [28].

Building the constitutive relations of granular materials with a multiscale approach requires the stress and strain tensors to be related on the micro-scale. Basically, a granular assembly with applied loads to boundary grains will evolve with the change of boundary conditions. The evolution of grains follows Newton's law, with repulsive forces between grains that are not nil when contact exists between grains. The boundary grains firstly move according to the mechanical imbalance. Thus, these displacements progressively disturb the internal balance according to Newton's second law and the granular assembly rearranges. As a consequence, the mechanical response of a granular assembly results from dynamical mechanisms governing the motion of each particle constrained by the existence of adjoining particles. This is exactly the leading principal of discrete element models [32]. However, a high degree of freedom in the resulting nonlinear differential equation system implies that it is merely impossible to obtain the analytical solution of the problem.

To simplify the differential equation system, some assumptions are introduced. In the micro-directional model, all grains of the granular assembly are considered to be spherical. The specimen is described as a distribution of contacts oriented along each direction of the physical space. All contact

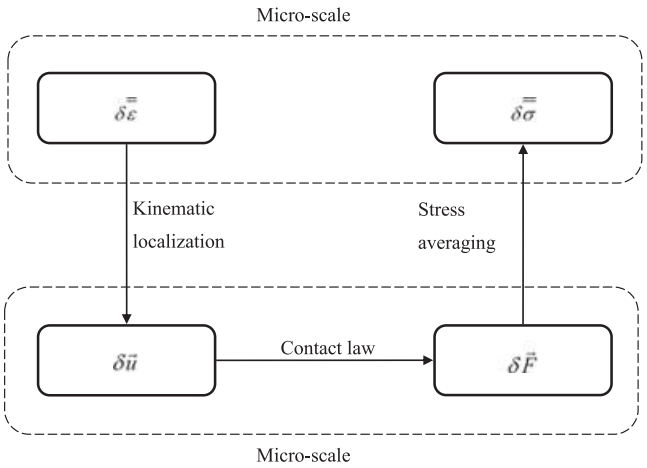

Figure 1. General homogenization scheme of the micro-directional model [26].

directions are independent of each other. Thus, the constitutive relation of the micro-directional model can be decomposed in three steps as shown in the general homogenization scheme (Figure 1),

(1) Kinematic localization: $\delta u_i\left(\vec{n}\right) = 2r_g \delta\varepsilon_{ij} n_j$ where δu_i is the incremental relative displacement with respect to the contact direction $\vec{n}$, r_g denotes the mean radius of the spherical grains, $\delta\varepsilon_{ij}$ is the incremental macrostrain tensor.

(2) Contact law: The local behavior is selected according to the granular material in hand. For granular soils, an elasto-perfect plastic model can be implemented, relating the local normal force F_n^c to the local normal relative displacement u_n^c as well as the local tangential force F_t^c to the local tangential relative displacement u_t^c. Besides, this contact law includes a Mohr–Coulomb criterion and can be expressed under the following incremental formalism, which introduces a normal elastic stiffness k_n and a tangential elastic stiffness k_t, both constant, and a local friction angle φ_g.

$$\begin{cases} \delta F_n^c = k_n \delta u_n^c \\ \delta \vec{F}_t^c = \min\left\{ \left\| \vec{F}_t^c + k_t \delta \vec{u}_t^c \right\|, \tan\varphi_g \left(F_n^c + \delta F_n^c \right) \right\} \times \frac{\vec{F}_t^c + k_t \delta \vec{u}_t^c}{\left\| \vec{F}_t^c + k_t \delta \vec{u}_t^c \right\|} - \vec{F}_t^c \end{cases} \tag{1}$$

(3) Stress averaging: The stress tensor for a representative elementary volume (REV) packing is homogenized based on the Love's formula [33–35]

$$\sigma_{ij} = \frac{1}{V} \sum_{c=1}^{N_c} F_i^c l_j^c \tag{2}$$

where $\vec{l}^c$ is the branch vector joining the centers of particles in contact on contact c, $\vec{F}^c$ is the contact force, and the sum is extended to all the Nc contacts occurring in the REV of volume V.

As an extension of the micro-directional model, the H-micro-directional model was developed to describe the constitutive relation of granular materials by taking into account the local geometrical interaction between grains [30]. The main limitation of the micro-directional model is that the deformation on the contact level corresponds to the strain on the macroscopic (specimen) scale. (the so-called affine approximation)

To overcome this limitation, a hexagon pattern (meso-scale) takes the place of the single contact to be the directional element constituting the material fabric on the meso-scale. The hexagon, as shown in Figure 2, consists of six particles with identical radius. A fundamental assumption of the hexagon pattern should be declared, that the hexagon is fully symmetric with respect to axis $\vec{n}$ and $\vec{t}$. The quasi-static equilibrium of the hexagon can be reached under the symmetric external forces. Thus, only the mechanical balance of two grains, denoted by grain 1 and 2, is needed to be solved.

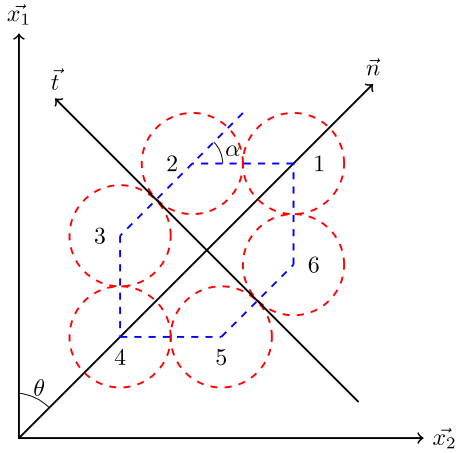

Figure 2. The hexagonal element of the H-directional model. [Colour figure can be viewed at wileyonlinelibrary.com]

The opening angle α embedded in the hexagon pattern is a significant parameter, highly relating the deformation and the void ratio of the hexagon. Different with the micro-directional model, particle rearrangement can be expressed by updating the opening angle in each hexagon, which evolves during the loading path.

3. THREE-DIMENSIONAL-H MODEL

The H-directional model is still limited within a 2D context. In order to extend the application range of the H-directional model, especially to implement it in 3D finite element method (FEM) codes, several questions are encountered, such as how to extend this striking 2D-H-directional model to 3D conditions. More generally, how to extend a 2D multiscale constitutive model to 3D conditions in a feasible and straightforward way? In this section, an innovative approach that is able to extend the 2D-H-directional model to 3D conditions is presented.

3.1. Kinematic localization

In 3D conditions, a global coordinate system $\left(\vec{x}_1, \vec{x}_2, \vec{x}_3\right)$ is required, where $\vec{x}_1, \vec{x}_2, \vec{x}_3$ axes stand for the principal stress directions on the macro-scale. The 3D-H model similarly follows the three steps shown in Figure 1, going from the incremental macroscopic strain tensor $\delta\bar{\bar{\varepsilon}}$ to the incremental macroscopic stress tensor $\delta\bar{\bar{\sigma}}$ by transforming the micro-scale and meso-scale information. No rotation of the principal axis of both stress and strain tensors is supposed to take place, so that $\delta\bar{\bar{\varepsilon}}$ and $\delta\bar{\bar{\sigma}}$ express as

$$\delta\bar{\bar{\varepsilon}} = \begin{bmatrix} \delta\varepsilon_{11} & 0 & 0 \\ 0 & \delta\varepsilon_{22} & 0 \\ 0 & 0 & \delta\varepsilon_{33} \end{bmatrix} \quad \delta\bar{\bar{\sigma}} = \begin{bmatrix} \delta\sigma_{11} & 0 & 0 \\ 0 & \delta\sigma_{22} & 0 \\ 0 & 0 & \delta\sigma_{33} \end{bmatrix} \tag{3}$$

The granular assembly is described as a distribution of meso-structures oriented along each direction of the physical space. As shown in Figure 3, each meso-structure with respect to a given local frame $\left(\vec{n}, \vec{t}, \vec{w}\right)$, which can be described by Euler angles θ, φ and ψ. Thus, a distribution function $\omega\left(\theta, \varphi, \psi\right)$ that indicates the density of meso-structures associated with the frame $\left(\vec{n}, \vec{t}, \vec{w}\right)$ is introduced. This function expresses the directional distribution of the meso-structures to describe texture arrangement of the granular assembly. In this paper, only the isotropic distribution is discussed.

The coordinate transformation from global frame to local frame can be implemented by employing the rotation matrix $\bar{\bar{P}}$, which is computed as the composition product of elementary rotation

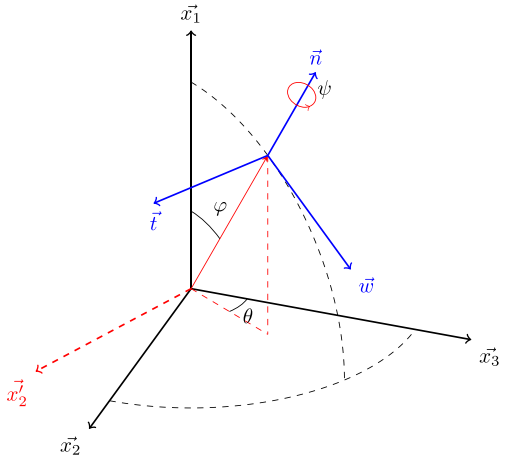

Figure 3. Global and local coordinate systems. [Colour figure can be viewed at wileyonlinelibrary.com]

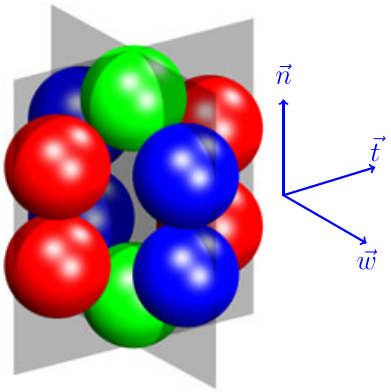

Figure 4. The meso-structure of 3D-H model. [Colour figure can be viewed at wileyonlinelibrary.com]

matrices along axis $\vec{x_1}$, $\vec{x_2'}$, and $\vec{n}$, respectively:

$$\bar{\bar{P}} = \begin{bmatrix} 1 & 0 & 0 \\ 0 & \cos\psi & -\sin\psi \\ 0 & \sin\psi & \cos\psi \end{bmatrix} \begin{bmatrix} \cos\varphi & 0 & -\sin\varphi \\ 0 & 1 & 0 \\ \sin\varphi & 0 & \cos\varphi \end{bmatrix} \begin{bmatrix} 1 & 0 & 0 \\ 0 & \cos\theta & -\sin\theta \\ 0 & \sin\theta & \cos\theta \end{bmatrix} \tag{4}$$

which gives

$$\bar{\bar{P}} = \begin{bmatrix} \cos\varphi & -\sin\theta\sin\varphi & -\cos\theta\sin\varphi \\ -\sin\varphi\sin\psi & \cos\theta\cos\psi - \sin\theta\cos\varphi\sin\psi & -\sin\theta\cos\psi - \cos\theta\cos\varphi\sin\psi \\ \sin\varphi\cos\psi & \cos\theta\sin\psi + \sin\theta\cos\varphi\cos\psi & -\sin\theta\sin\psi + \cos\theta\cos\psi\cos\varphi \end{bmatrix} \tag{5}$$

Besides, the meso-structure introduced in the following section (Figure 4) is a significant connection between macro-scale and meso-scale. The branch vector relies the centers of particles in contact: $\vec{L} = [l_1, l_2, l_3]^T$, wherein l_1, l_2, l_3 represent the lengths along directions $\vec{n}$, $\vec{t}$, $\vec{w}$, respectively. Thus, the kinematic localization gives

$$\delta\vec{L} = \bar{\bar{P}}\delta\bar{\bar{\varepsilon}}\bar{\bar{P}}^{-1}\vec{L} \tag{6}$$

where $\delta\vec{L} = \begin{bmatrix} \delta l_1 \\ \delta l_2 \\ \delta l_3 \end{bmatrix}$

3.2. Meso-structure behavior

The meso-structure is composed of 10 spherical grains with the identical radius r_g (Figure 4). This meso-structure is selected because it includes a grain cluster, large enough to contain four force chains, and enabling grain rearrangement. It can be described analytically, and solved by hand, which is a great advantage. The grain centers respectively belong to two mutually perpendicular planes. Meanwhile, the centers of grains make up two mutually perpendicular hexagon patterns. Thus, the meso-structure can be decomposed into two independent hexagon patterns: Hexagon A and Hexagon B (shown in Figures 5 and 6). To inherit the features from the H-directional model, this meso-structure is able to lead complicated kinematic mechanisms, including local dilatant and contractant behaviors. To simplify the derivation, it is assumed that each meso-structure is subjected to an external symmetric load. Consequently, only two contacts between grains 1 to 2 and grains 2 to 3, respectively denoted by contact 1 and contact 2, are considered in Hexagon A, while two contacts between grains 1 to 7 and grains 7 to 8, denoted by contact 3 and contact 4, are considered in Hexagon B. T_1 is tangential component and N_1 is normal component of the contact force of contact 1. The contact force applied by grain 3 to grain 2 only involves a normal component N_2; the tangential component is nil because of the symmetry. The relative incremental displacement between

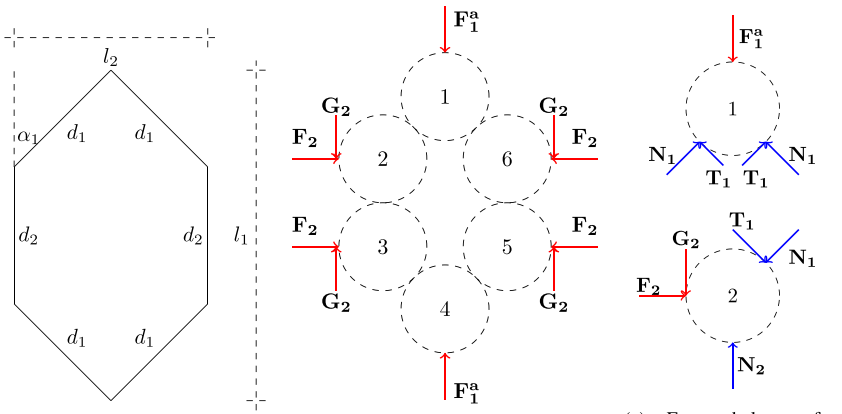

(a) Branch vector (b) External forces (c) Force balance for grains 1 and 2

Figure 5. Mechanical description of hexagon pattern A. (a) Branch vector, (b) external forces, and (c) force balance for grains 1 and 2. [Colour figure can be viewed at wileyonlinelibrary.com]

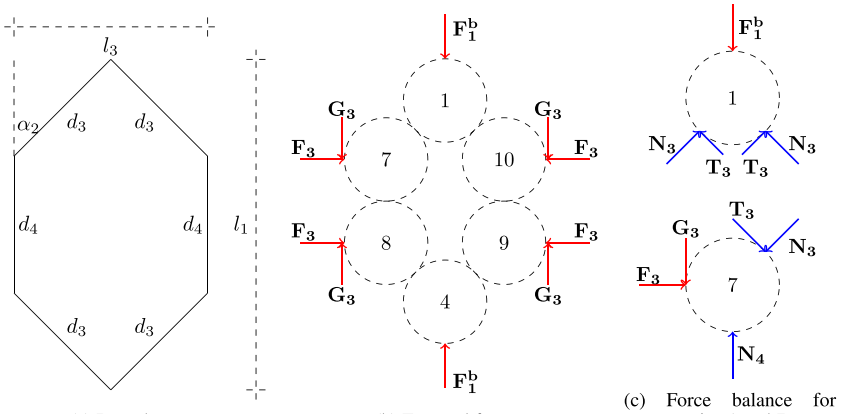

(a) Branch vector (b) External forces (c) Force balance for grains 1 and 7

Figure 6. Mechanical description of hexagon pattern B. [Colour figure can be viewed at wileyonlinelibrary.com]

grains 2 and 3 is composed of a normal component δu_n^1 and a tangential component δu_t^1. Likewise, the relative incremental displacement of contact 2 is composed of a single normal component. Employing the notations given in Figure 5(a), it follows that

$$\begin{aligned} \delta u_n^1 &= \delta d_1 \\ \delta u_t^1 &= d_1 \delta \alpha_1 \\ \delta u_n^2 &= \delta d_2 \end{aligned} \tag{7}$$

The geometrical compatibility yields

$$\begin{aligned} l_1 &= d_2 + 2d_1 \cos \alpha_1 \\ l_2 &= 2d_1 \sin \alpha_1 \end{aligned} \tag{8}$$

Force balance of grain 1 along direction $\vec{n}$ and of grain 2 along direction $\vec{w}$ and $\vec{n}$ and moment balance of grain 2 reads

$$F_1^a = N_1 \cos \alpha_1 + T_1 \sin \alpha_1 \tag{9a}$$

$$F_2 = N_1 \sin \alpha_1 - T_1 \cos \alpha_1 \tag{9b}$$

$$N_2 = N_1 \cos\alpha_1 + T_1 \sin\alpha_1 + G_2 \tag{9c}$$

$$G_2 = T_2 \tag{9d}$$

It should be noted that no rolling is assumed to affect particles (Equation (9d)). This assumption is undoubtedly questionable for spherical-shaped grains, where particle rolling acts as an important ingredient of the deformational processes [36]. However, it seems to be reasonable for real granular soil materials where actual grains are angular with multiple facets [37, 38].

The inter-particle contact law expressed in Equation (1) is employed. After simplifying (see detail in Appendix A), Equation (1) can be rewritten as follows:

$$\begin{aligned} \delta N_i &= -k_n \delta d_i \\ \delta T_i &= B_i \delta\alpha_j - A_i \delta d_i + C_i \end{aligned} \qquad i = 1, 2, 3, 4 \tag{10}$$

For the purpose of simplification, term C_i is negligible. It differs from zero only during a transition from elastic regime to plastic regime. Except this situation, it is zero. For very small strain increments, as considered throughout this paper, term C_i can therefore be neglected.

To obtain the incremental evolution of the external forces, δd_1, δd_2, and $\delta\alpha_1$ have to be expressed as a function of the meso strain. Three equations are therefore required. Compatibilities (Equation (8)) provide two relations. The third one is the balance equation of grain 2 along direction $\vec{n}$ (Equation (9c)). Taking the inter-particle contact law (Equation (10)) into account leads to the following algebraic system expressing the incremental changes in δd_1, δd_2, and $\delta\alpha_1$ with respect to the incremental changes in δd_1 and δd_2:

$$\begin{bmatrix} 2\cos\alpha_1 & 1 & -2d_1\sin\alpha_1 \\ 2\sin\alpha_1 & 0 & 2d_1\cos\alpha_1 \\ \cos\alpha_1 + \frac{A_1}{k_n}(\sin\alpha_1 + 1) & -1 & \frac{F_2 - B_1(\sin\alpha_1+1)}{k_n} \end{bmatrix} \begin{bmatrix} \delta d_1 \\ \delta d_2 \\ \delta\alpha_1 \end{bmatrix} = \begin{bmatrix} \delta l_1 \\ \delta l_2 \\ 0 \end{bmatrix} \tag{11}$$

where A_1, B_1 are given in Appendix A.

Differentiating Equations (9a), (9b) and combining with Equation (10) gives

$$\begin{aligned} \delta F_1^a &= -k_n \cos\alpha_1 \delta u_n^1 + k_t \sin\alpha_1 \delta u_t^1 - F_2 \delta\alpha_1 \\ \delta F_2 &= -k_t \cos\alpha_1 \delta u_t^1 - k_n \sin\alpha_1 \delta u_n^1 + F_1^a \delta\alpha_1 \end{aligned} \tag{12}$$

Thus, combining Equations (7), (11), and (12), the incremental constitutive relation for Hexagon A can be expressed as follows:

$$\frac{1}{|D|^a} \begin{bmatrix} K_{11}^a & K_{12}^a \\ K_{21}^a & K_{22}^a \end{bmatrix} \begin{bmatrix} \delta l_1 \\ \delta l_2 \end{bmatrix} = \begin{bmatrix} \delta F_1^a \\ \delta F_2 \end{bmatrix} \tag{13}$$

Similarly, the incremental constitutive relation for Hexagon B reads:

$$\frac{1}{|D|^b} \begin{bmatrix} K_{11}^b & K_{12}^b \\ K_{21}^b & K_{22}^b \end{bmatrix} \begin{bmatrix} \delta l_1 \\ \delta l_3 \end{bmatrix} = \begin{bmatrix} \delta F_1^b \\ \delta F_3 \end{bmatrix} \tag{14}$$

Finally, superimposing Hexagon A and Hexagon B, the total incremental force along direction $\vec{n}$ is $\delta F_1 = \delta F_1^a + \delta F_1^b$. The incremental constitutive relation of the 3D meso-structure can be obtained as follows: (see detail in Appendix B)

$$\bar{\bar{K}} \delta\vec{l} = \delta\vec{F} \tag{15}$$

with $\bar{\bar{K}} = \begin{bmatrix} \frac{1}{|D|}^a K_{11}^a + \frac{1}{|D|^b} K_{11}^b & \frac{1}{|D|^a} K_{12}^a & \frac{1}{|D|^b} K_{12}^b \\ \frac{1}{|D|^a} K_{21}^a & \frac{1}{|D|^a} K_{22}^a & 0 \\ \frac{1}{|D|^b} K_{21}^b & 0 & \frac{1}{|D|^b} K_{22}^b \end{bmatrix}$

3.3. Stress averaging

Averaging the mesostress taking place within all the meso-structures in the specimen of volume V can be performed as follows:

$$\bar{\bar{\sigma}} = \frac{1}{V} \iiint \omega(\theta, \varphi, \psi) \bar{\bar{P}}^{-1} \tilde{\bar{\sigma}}(\vec{n}, \vec{t}, \vec{w}) \bar{\bar{P}} \sin\varphi d\varphi d\theta d \tag{16}$$

where $\bar{\bar{\sigma}}$ is the macro-stress tensor operating on the specimen scale. For an isotropic specimen, the distribution function $\omega(\theta, \varphi, \psi)$ is constant and $\theta \in [0, 2\pi)$, $\varphi \in [0, \pi]$, $\psi \in [0, 2\pi)$ (θ, φ, ψ are the Euler angles depicted in Figure 3). The mesostress $\tilde{\bar{\sigma}}(\vec{n}, \vec{t}, \vec{w})$ with respect to the local frame can be computed using the Love–Weber's formula [33–35, 39]:

$$\begin{aligned}
\tilde{\sigma}_{11}(\vec{n}, \vec{t}, \vec{w}) &= 4N_1 d_1 \cos^2\alpha_1 + 4T_1 d_1 \cos\alpha_1 \sin\alpha_1 + 2N_2 d_2 \\
&\quad + 4N_3 d_3 \cos^2\alpha_2 + 4T_3 d_3 \cos\alpha_2 \sin\alpha_2 + 2N_4 d_4 \\
\tilde{\sigma}_{22}(\vec{n}, \vec{t}, \vec{w}) &= 4N_1 d_1 \sin^2\alpha_1 - 4T_1 d_1 \cos\alpha_1 \sin\alpha_1 \\
\tilde{\sigma}_{33}(\vec{n}, \vec{t}, \vec{w}) &= 4N_3 d_3 \sin^2\alpha_2 - 4T_3 d_3 \cos\alpha_2 \sin\alpha_2 \\
\tilde{\sigma}_{ij}(\vec{n}, \vec{t}, \vec{w}) &= 0 \quad \text{when} \quad i \neq j
\end{aligned} \tag{17}$$

It should be mentioned that a classical approximation is introduced when averaging the stress: the applied point of each external force is shifted from the grain boundary to the grain center, making it possible to introduce the branch vectors, and to retrieve the usual Love–Weber formula (see [40] for details).

The principal components of meso-stress tensor are calculated by the internal forces and the geometric terms of the meso-structure. Besides, off-diagonal components can be simply considered as nil, because the meso-structure with respect to $(\vec{n}, \vec{t}, \vec{w})$ always offsets the one with respect to $(-\vec{n}, -\vec{t}, -\vec{w})$ in off-diagonal components when integrated. This point is also validated from a numerical point of view.

3.4. Opening angle and void ratio

For a virgin specimen, the initial opening angle is denoted α_0. Then, $\alpha_1 = \alpha_2 = \alpha_0$. The initial void ratio $e_0(\vec{n}, \vec{t}, \vec{w})$ of each meso-structure belonging to local frame $(\vec{n}, \vec{t}, \vec{w})$ can be estimated by using the initial opening angle α_0. The volume of the dodecahedron that is made up of the branch vectors of meso-structure can be expressed as follows:

$$V_{d12} = 32 r_g^3 \sin^2\alpha_0 \left(\frac{1}{3} \cos\alpha_0 + \frac{1}{2} \right) \tag{18}$$

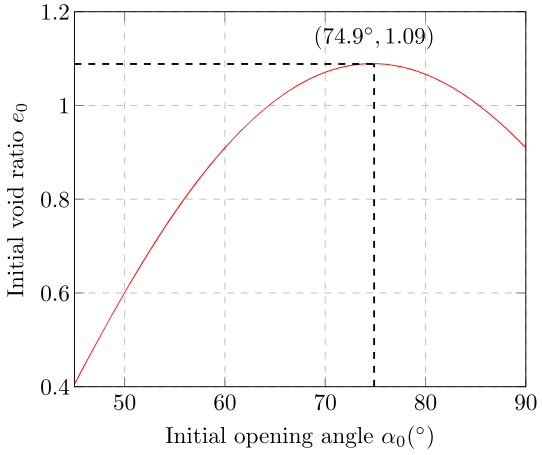

Figure 7. Evolution of initial void ratio as a function of initial opening angle. [Colour figure can be viewed at wileyonlinelibrary.com]

where r_g is grain radius; α_0 is the initial opening angle of the meso-structure considered.

The volume of the solid V_{s12} in the dodecahedron includes 10 parts. It is easy to calculate the entire volume of the solid, because the volume of the five parts on top side equal the volume of a whole grain. Thus, the entire volume of the solid parts can be calculated as follows:

$$V_s = \frac{8}{3}\pi r_g^3 \tag{19}$$

Combining Equations (18) and (19), the initial void ratio expression is given by

$$e_0 = \frac{V_{d12} - V_s}{V_s} == -\frac{4}{\pi}\cos^3\alpha_0 - \frac{6}{\pi}\cos^2\alpha_0 + \frac{4}{\pi}\cos\alpha_0 + \frac{6}{\pi} - 1 \tag{20}$$

The evolution of e_0 with respect to angle α_0 (Equation (20)) is plotted in Figure 7; the initial opening angle α_0 is limited because of initial configuration of the meso-structure without overlapping between grains. The minimum value $\alpha_0 = 45°$ corresponds to the condition that the grain 2 is just in contact with grains 7 and 10. The maximum value can reach 90° when the grains 1 and 4 are touching. In order to estimate the initial opening angle from the initial void ratio, Equation (20) is required to become a bijective function. Thus, the domain of α_0 is limited from 45° to 74.9° corresponding to the initial void ratio e_0 from 0.4 to 1.09. Consequently, α_0 can be estimated from e_0, which is obtained from laboratory test. With the help of this key micro parameter α_0, the geometric fabric of the meso-structure is determined. However, it should be noted that the maximum and minimum values of e_0 are not the maximum and minimum void ratios of the specimen considered.

4. PERFORMANCES OF THE THREE-DIMENSIONAL-H MODEL

In this section, the performance of the 3D-H model is examined. First, parameters are calibrated by comparing the numerical response of the model with experimental data. Second, one of the most appropriate set of parameters is adopted to carry out prediction tests at different confining pressures. Then, some numerical simulations are conducted along different loading paths. As discussed in the previous section, the proposed model introduces four parameters: k_n, k_t, φ_g (material parameters), and e_0, wherein the initial void ratio e_0 corresponding to opening angle α_0 can be estimated from Equation (20).

4.1. Parameter calibration and model prediction

The calibration of the present model can be performed from the comparison between numerical and experimental results. The experiment was carried out along the conventional drained triaxial loading path with mono-disperse sand ($d_{50} = 0.6$ mm) called Ticino sand, well characterized from a geotechnical point of view and adopted in many studies [41].

Conventional triaxial compression test at 200 kPa of confining pressure is adopted to calibrate the model parameters by considering two responses: (1) the stress–strain response; (2) the volumetric

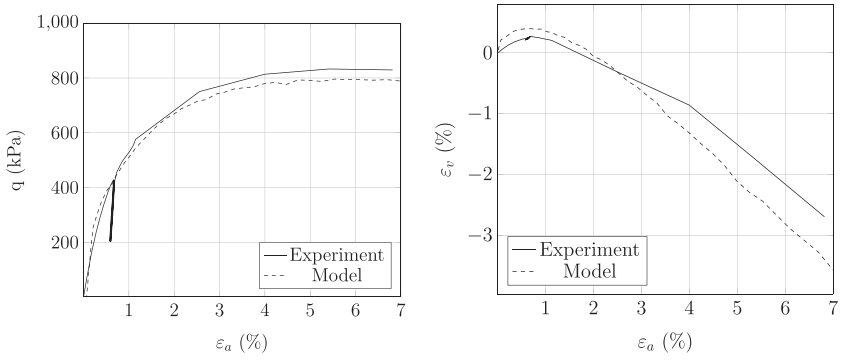

(a) Deviatoric stress versus axial strain.

(b) Volumetric strain versus axial strain

Figure 8. Calibration phase of the model at 200 kPa of confining pressure.

Table I. Parameters selected in calibration and prediction phases.

k_n(N/m)	k_t(N/m)	e_0	φ_g(°)	Initial isotropic stress p_0(kPa)
1.90×10^6	1.14×10^6	0.53	25	100, 200, 300 and 400

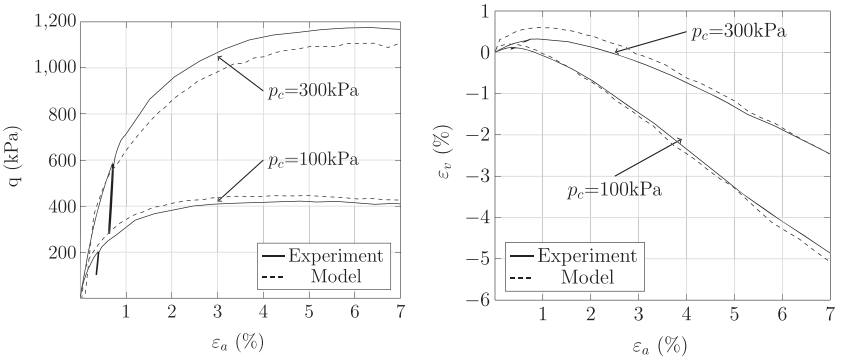

(a) Deviatoric stress versus axial strain

(b) Volumetric strain versus axial strain

Figure 9. Prediction capability of the model at 100 and 300 kPa of confining pressures. (a) Deviatoric stress versus axial strain and (b) volumetric strain versus axial strain.

response. Figure 8 shows the numerical result in comparison with the experimental result, where the experimental curves are well reproduced using the set of parameters reported in Table I.

Figure 9 shows the model predictions of deviatoric stress and volumetric strain plotted against axial strain at different confining pressures. The calibrated parameters reported in Table I are employed. Evidently, the model predictions agree fairly well with the experimental curves in terms of both the stress–strain relation and volumetric responses. As shown in Figure 9(a), the numerical curve rises lower than the experimental curve at 300 kPa of confining pressure while higher at 100 kPa. Figure 9(b) plots the volumetric strain ε_v versus axial strain ε_a. The experimental curves are accurately reproduced especially when $\varepsilon_a < 4\%$, but experience more dilatancy for larger axial strains.

In general, the calibration and prediction evidence satisfying results. The present model captures well the experimental curves with only four parameters. A key geometrical parameter α_0 evolves independently during loading paths, which will be further discussed subsequently.

4.2. Triaxial loading paths

Conventional triaxial compression tests at different confining pressures are selected to show how the proposed model simulates the behavior observed for sands. For demonstration purpose, the simulations at 100, 200, and 400 kPa confining pressures are compared in Figure 10 from $\varepsilon_a = 0\%$ to $\varepsilon_a = 25\%$. The parameters reported in Table I are adopted.

Figure 10(a) shows that the deviatoric stress q reaches a peak at a small strain about $\varepsilon_a = 5\%$ and undergoes a subsequent softening regime until critical state. As shown in Figure 10(b), the deviatoric stress q triple increases as the mean stress p during the triaxial loading path. The volumetric strain responses at different confining pressures are displayed in Figure 10(c), where a dilatancy can be observed before the critical state, except a sensible contractancy captured at the beginning. Figure 10(d) plots the void ratio e versus the mean stress p in logarithms form. The curves are increasing until the critical state line. The evolution of the void ratio can be observed in Figure 10(e) where the volumetric strains ε_v firstly decrease and then increase until a plateau is reached. Figure 10(f) gives the deviatoric ratios q/p plotted against the axial strain ε_a. The peak of deviatoric stress ratio increases as the initial confining pressure decreases. All the curves converge toward more or less the same value, close to 1.25. In 3D conditions, the deviatoric ratio is related to

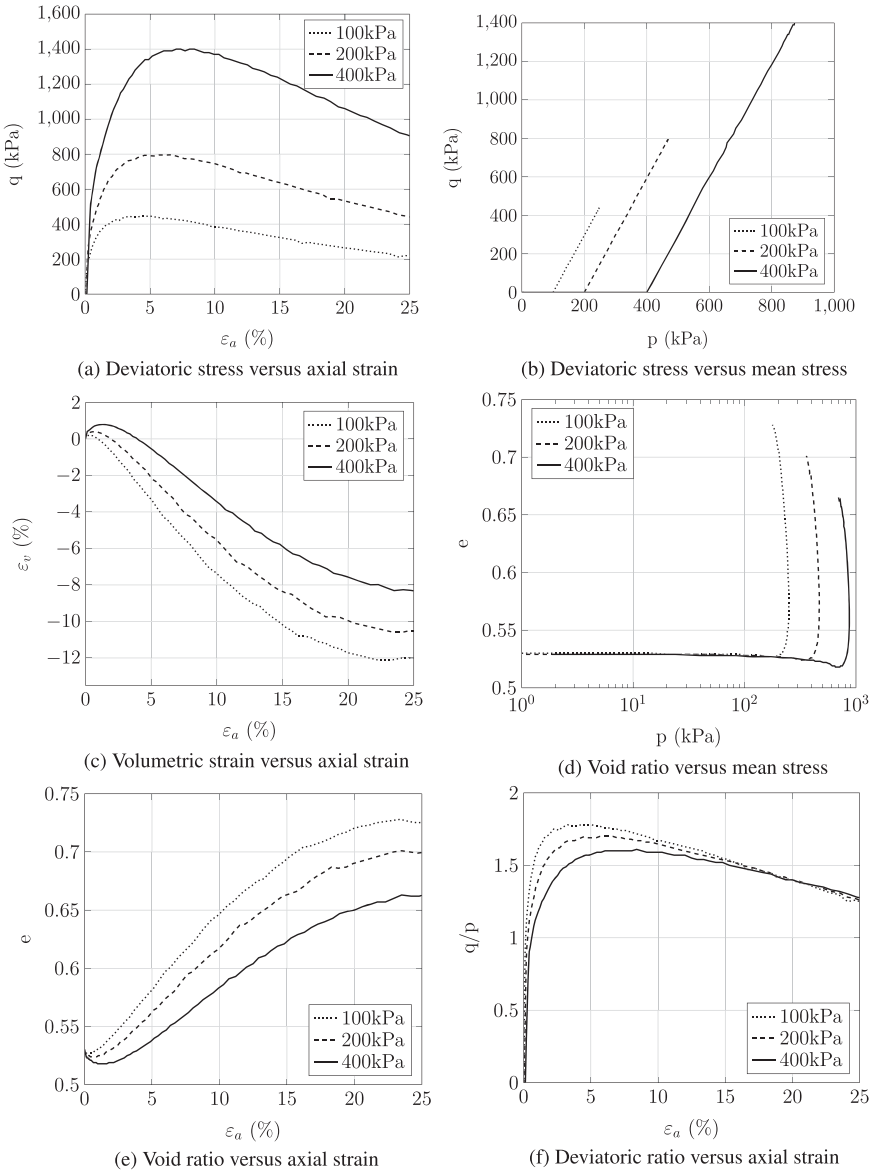

(a) Deviatoric stress versus axial strain

(b) Deviatoric stress versus mean stress

(c) Volumetric strain versus axial strain

(d) Void ratio versus mean stress

(e) Void ratio versus axial strain

(f) Deviatoric ratio versus axial strain

Figure 10. Effect of different initial confining pressures on model responses along an axisymmetric drained triaxial loading path. (a) Deviatoric stress versus axial strain, (b) deviatoric stress versus mean stress, (c) volumetric strain versus axial strain, (d) void ratio versus mean stress, (e) void ratio versus axial strain and (f) deviatoric ratio versus axial strain.

the mobilized macroscopic friction angle, as

$$\frac{q}{p} = \frac{6\sin\varphi_c}{3-\sin\varphi_c} \tag{21}$$

which gives $\varphi_c \sim 31.15°$ when $q/p = 1.25$

Besides, additional three CTC tests are carried out at a same initial confining pressure, namely, 200 kPa, but different initial void ratios $e_0 = 0.43$, $e_0 = 0.53$, $e_0 = 0.63$. As shown in Figure 11(a), the deviatoric stress q reaches different peaks because of the effect of different initial void ratios. The peak of the curve corresponding to $e_0 = 0.53$ (the densest specimen) rises higher than the curve corresponding to $e_0 = 0.63$ (the loosest specimen). In Figure 11b, the void ratio slightly decreases at the beginning and then increases until the critical void ratio at the end, where a convergence tendency can be observed. Conversely, the loosest specimen reaches a higher critical void ratio than

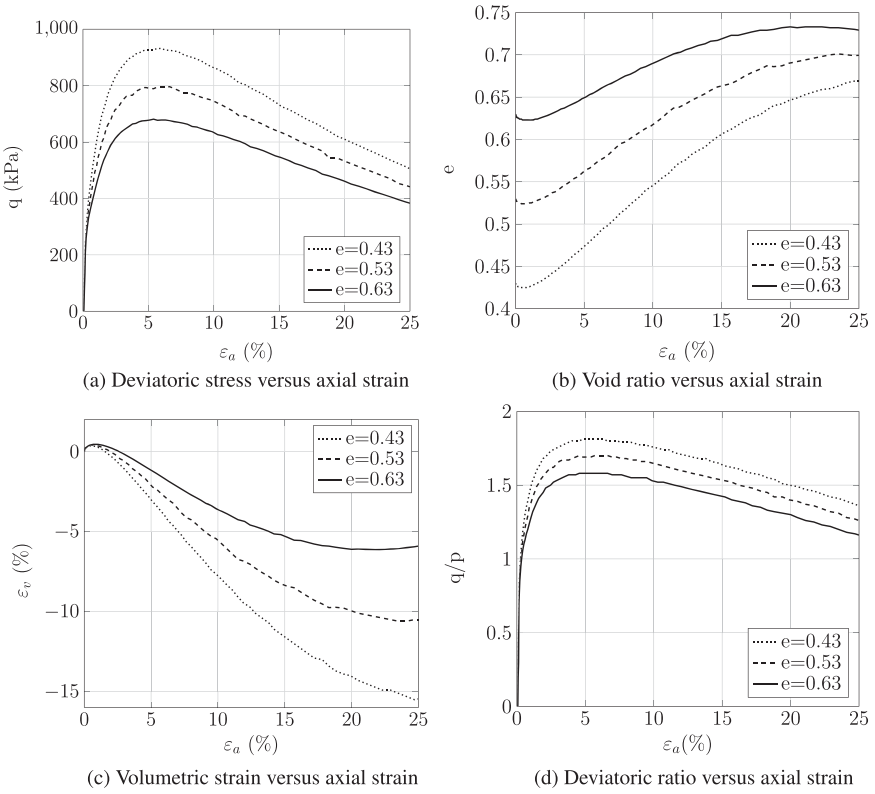

(a) Deviatoric stress versus axial strain

(b) Void ratio versus axial strain

(c) Volumetric strain versus axial strain

(d) Deviatoric ratio versus axial strain

Figure 11. Effect of different initial void ratios on the model response along an axisymmetric drained triaxial loading path.

the densest one. As shown in Figure 11(c), the volumetric strain curves decrease before $\varepsilon_a = 2\%$ and increase until critical state. The densest specimen response is more dilatant than that of the loosest one. Figure 11 plots the axial strains versus the deviatoric ratios, which shows that the largest initial void ratio brings out the lowest peak in deviatoric ratio q/p, corresponding to the highest macroscopic friction angle φ_c. It is very challenging for a stress–strain model to reproduce the critical state, when no specific assumptions are introduced. However, by the proposed model it is observed that the critical state is not perfectly obtained, but is reached approximately.

It is noticed that the hardening and softening behavior, including the qualitatively described critical state, can be better illustrated from a micro-mechanical point of view. The 3D distributions of micro variables including micro stresses ($\tilde{\sigma}$), contact information, and opening angles ($\alpha_{1(2)}$) involve three Euler angles (θ, φ, and ψ; Figure 3). For the purpose of simplification, these 3D micro variables can be integrated either over φ, ψ or over θ, ψ. Considering the drained triaxial loading path, the former is selected. The angular distributions of micro variables at different strain states, with 200 kPa confining stress are illustrated along angle θ in Figure 12. In each sub-figure, three polar figures are shown: the integrated micro stress $\iint \omega\tilde{\sigma_n} d\theta d\psi$, $\iint \omega\tilde{\sigma_t} d\theta d\psi$, and $\iint \omega\tilde{\sigma_w} d\theta d\psi$ (left column); the percentage of plastic or buckling meso-structures (center column); the mean normalized opening angle ($\alpha_1/\alpha_0, \alpha_2/\alpha_0$) (right column). It should be mentioned that the buckling area in the center column denotes the percentage of total number of meso-structures in a certain value of θ. As a meso-structure is buckling, $\tilde{\sigma}$ and $\alpha_{1(2)}$ are set to zero. The contact buckling is a significant feature of the present model, which enables it to simulate the persisting loss of contacts corresponding to the so-called force-chains buckling.

Initially, all of the meso-structures are created as isotropic distribution with same initial opening angle $\alpha_0 = 41.56°$. Figure 12(a) corresponds to the end of the isotropic compression phase, where the micro stresses and opening angle are isotropic distributed. Each meso-structure evolves independently, giving rise to different local relative displacements in terms of the kinematic local-

ization (Figure 6). During the isotropic compression phase, no buckling and plastic meso-structure can be observed, which indicates that the specimen still behaves in an elastic regime. As shown in Figure 12(b), $\iint \omega \tilde{\sigma_n} d\theta d\psi$ plays a major role along the axial compression direction ($\varphi = 0$ or 180°), which shows an anisotropic micro stress state. The meso-structures oriented within a central cone (angle β, the circumferential angle of the buckling cone) become buckling, because the meso-structures in this cone dilate too much in order to keep the constant confining stress. Meanwhile, more than 20% of meso-structures reach plastic regime in the rest of the area. Afterwards, Figure 12 (c, d, e, and f) shows the evolution of micro variables during the triaxial loading path. In the left column, micro stress increases in the non-buckling area as β also increases in the center column.

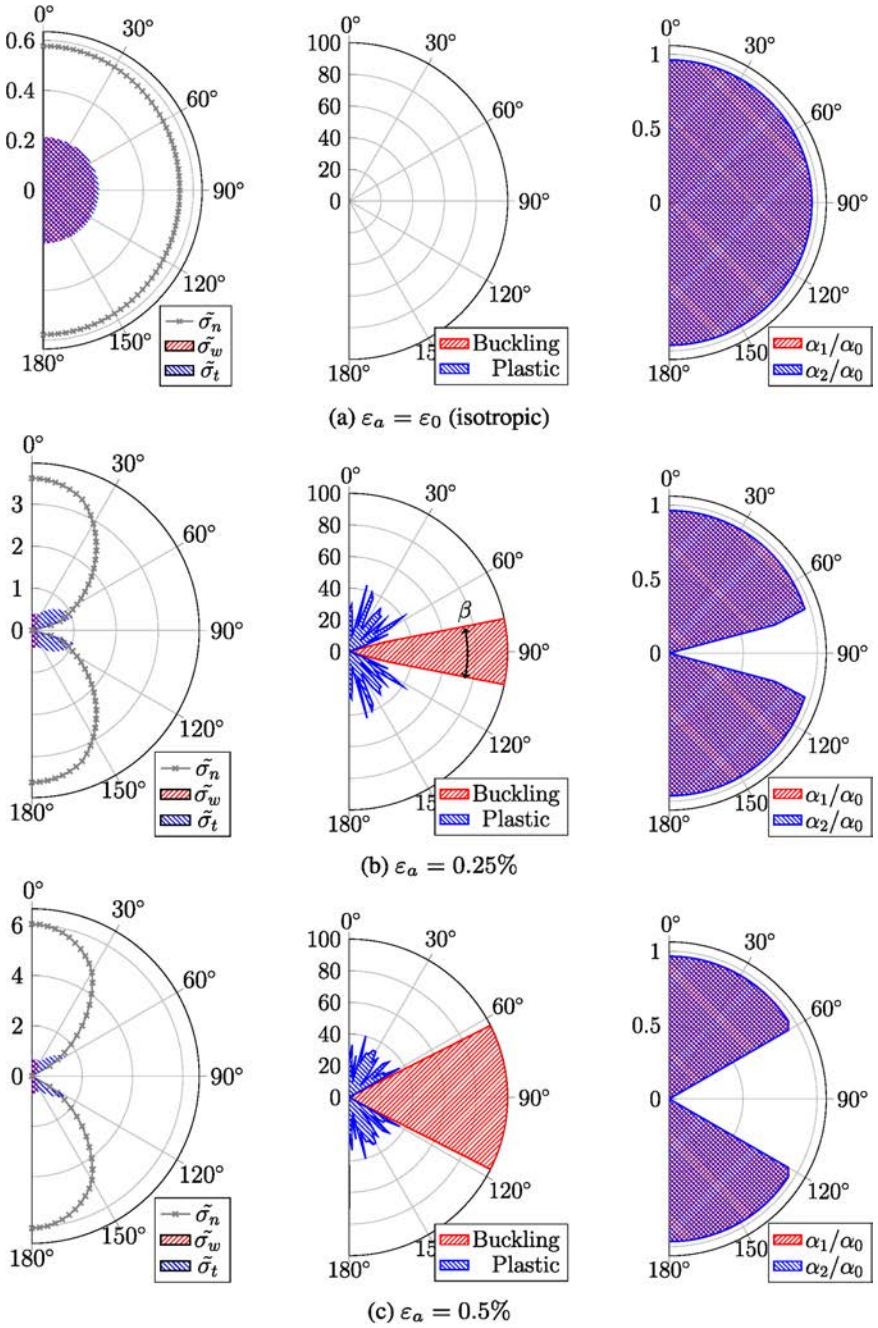

Figure 12.

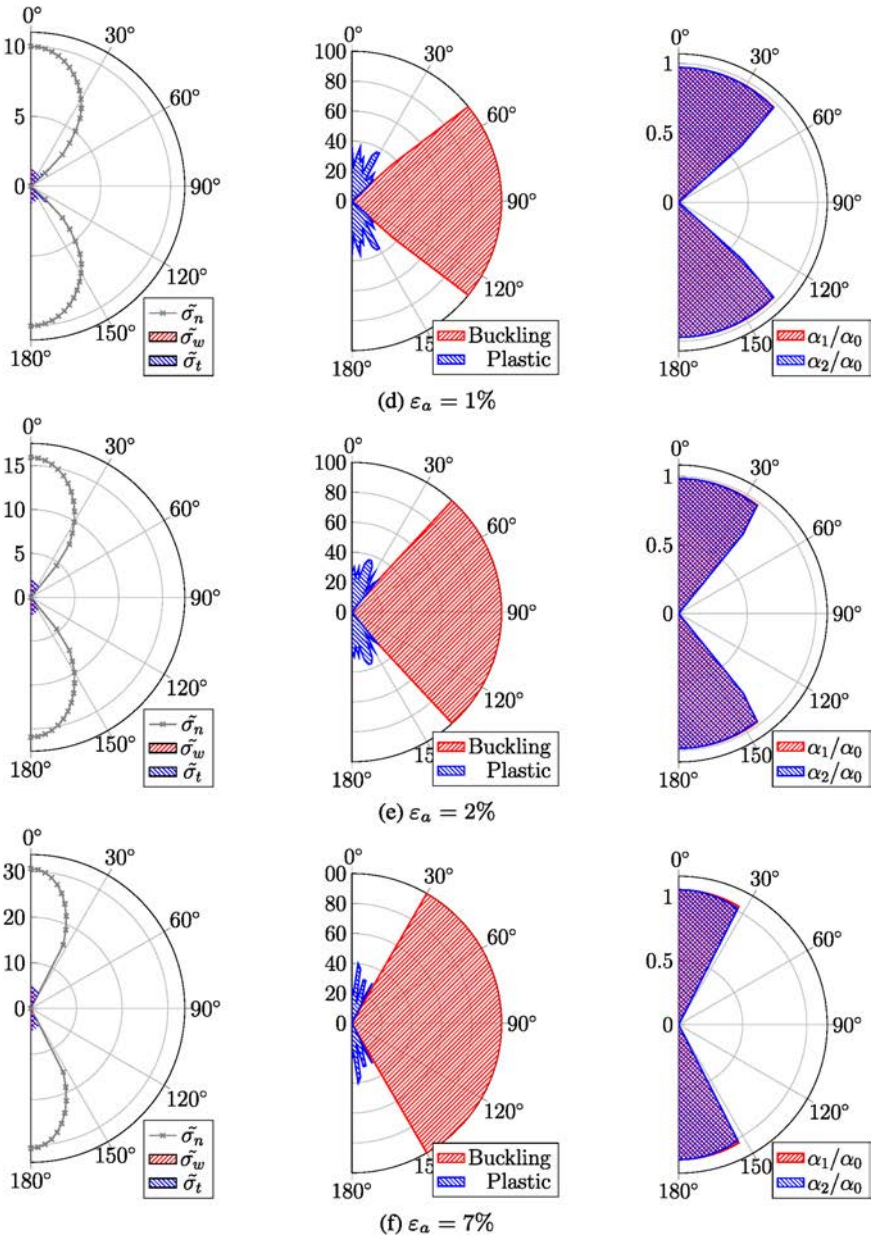

Figure 12. Angular distributions of micro variables along θ at different strain states, with 200 kPa of the confining stress: the integrated micro stress $\iint \omega\tilde{\sigma_n} d\theta d\psi$, $\iint \omega\tilde{\sigma_t} d\theta d\psi$, and $\iint \omega\tilde{\sigma_w} d\theta d\psi$ (N) (left column); the percentage of plastic or buckling meso-structures (center column); the mean normalized of the opening angles ($\alpha_1/\alpha_0, \alpha_2/\alpha_0$) (right column). [Colour figure can be viewed at wileyonlinelibrary.com]

Thus, the macro stress–strain response can be better illustrated from these micro state variables. If the micro stress increasing plays a major role, the macro-stress raises. Otherwise, if the buckling regime plays a major role, the macro-stress decreases. Moreover, the increasing and decreasing tendencies of the macro-stress can be reached a balance corresponding to the macro-stress plateau. Both buckling and plastic regimes of the present model cannot be reversed, which directs the softening behavior observed on the macro-scale. Additionally, slight growth of opening angle α_2 and α_3 can be observed in the right column. It is a key geometrical parameter, which has a tremendous influence on the micro forces of the meso-structure. This geometrical parameter also reveals the rearrangement of the specimen. The relative position between particles is obtained not only from the single contact relation, but also from the geometrical configuration described by this key parameter.

5. CONCLUSIONS AND PERSPECTIVES

Based on the homogenization scheme used in the micro-directional model and the H-directional model, the latter is extended to 3D conditions by replacing the 2D hexagonal pattern with a 3D meso-structure. For this purpose, a decomposition and superposition approach is introduced to analyze the local behavior of the meso-structure. The 3D-H model only introduces four parameters, wherein k_n, k_t, and φ_g stem from the elastic-perfect plastic inter-particle contact law. The other one (the opening angle α_0) is a key microscopic geometrical parameter that can be estimated from the initial void ratio. It is noteworthy that the granular assembly rearrangement can be reflected by the evolution of the opening angle α_0.

By comparing with experimental results on Ticino sands, the calibration of the model is carried out and the predictive capabilities are examined along drained triaxial compression loading paths. The results obtained are both qualitatively and quantitatively satisfying. The hardening and softening regimes are well reproduced in the stress–strain response. Meanwhile, the dilatant and contractant regimes are also described well with the volumetric strain curve. By adopting the calibrated parameters, two sets of numerical tests are run, including different confining stresses and initial void ratios. One of the most significant findings emerging from this study is that the critical state can be approximately described from void ratio evolution without involving any critical state line (CSL) formulations and parameters. The model mechanism is also analyzed from a microscopic point of view. The angular distributions of micro variables are plotted at different strain states under the drained triaxial loading path.

Further research could also be conducted to investigate the three following aspects:

(1) The response of the model with respect to both the strength and the volumetric behavior closely depend on the geometrical pattern used. In particular, it is thought that enriching this pattern, to include more important particle rearrangement, should give rise to a more markedly observed critical state property.
(2) Addressing the erosion and suffusion issues through a multiscale approach, as some additional particles can penetrate inside the meso-structure or can be removed (because of any external loading, as a fluid flow for example). The mechanical equilibrium of meso-structure need to be reconsidered. Thus, the erosion and suffusion phenomena could be simulated by considering the micro properties of adding or removing some additional particles on the micro-scale.
(3) Solving boundary value problems, once the 3D-H model is implemented in an FEM code. Each Gauss integration point in the FEM mesh represents a REV of 3D-H model. The FEM is considered to solve the boundary value problem on the macro-scale, while the 3D-H model is used to capture and describe effectively the constitutive behavior on the micro-scale.

APPENDIX A: CONTACT LAW

This elastic-perfect plastic model includes a Mohr–Coulomb criterion and can be expressed under the following incremental formalism by employing the notations depicted in Figures 5 and 6:

$$\begin{cases} \delta N_i = k_n \delta u_n^i \\ \delta T_i = \min\left\{ \left\| T_i + k_t \delta u_t^i \right\|, \tan\varphi_g \left(N_i + k_n \delta u_n^i \right) \right\} \times \frac{T_i + k_t \delta u_t^i}{\left\| T_i + k_t \delta u_t^i \right\|} - T_i \end{cases} \tag{A1}$$

where $i = 1, 2, 3, 4$ denotes the identifier of contact number.

According to Equation (7), Equation (A1) can be rewritten as follows:

$$\begin{cases} \delta N_i = -k_n \delta d_i \\ \delta T_i = k_t d_i \delta \alpha_j & \text{elastic regime} \\ \delta T_i = \tan\varphi_g \left(N_i - k_n \delta d_i \right) \xi_i - T_i & \text{plastic regime} \end{cases} \tag{A2}$$

where ξ_i is the sign of $T_i + k_t d_i \delta \alpha_j$; $j = 1$ when $i = 1, 2$; $j = 2$ when $i = 3, 4$; plastic regime is reached when $\| k_t d_i \delta \alpha_j + T_i \| \geq \tan\varphi_g \left(N_i - k_n \delta d_i \right)$, otherwise it is in elastic regime.

To facilitate the derivation, I_i^p and I_i^e are introduced as indicator functions of the contact state, expressed as follows:

$$I_i^p = \begin{cases} 1 & \text{in plastic regime} \\ 0 & \text{in elastic regime} \end{cases}; \quad I_i^e = 1 - I_i^p \tag{A3}$$

Thus, the constitutive relations can be expressed as follows:

$$\begin{cases} \delta N_i = -k_n \delta d_i \\ \delta T_i = B_i \delta \alpha_j - A_i \delta d_i + C_i \end{cases} \tag{A4}$$

$$\text{where} \begin{cases} A_i = I_i^p k_n \xi_i \tan \varphi_g \\ B_i = I_i^e k_t d_i \\ C_i = I_i^p (\xi_i \tan \varphi_g N_i - T_i) \end{cases}$$

APPENDIX B: STIFFNESS MATRIX ON THE MESO-SCALE

For Hexagon A, combining Equations (7) and (12) gives

$$\begin{cases} \delta F_1^a = -k_n \cos\alpha_1 \delta d_1 + (k_t \sin\alpha_1 d_1 - F_2)\, \delta\alpha_1 \\ \delta F_2 = -k_n \sin\alpha_1 \delta d_1 + \left(F_1^a - k_t \cos\alpha_1 d_1\right) \delta\alpha_1 \end{cases} \tag{B1}$$

Based on Equations (11), δd_1 and $\delta\alpha_1$ can be expressed as follows:

$$\begin{cases} \delta d_1 = \frac{1}{|D|^a} \left(2d_1 \cos\alpha_1 \delta l_1 + \frac{B_1}{k_n} \sin\alpha_1 \delta l_2 + \frac{B_1}{k_n} \delta l_2 - \frac{F_2}{k_n} \delta l_2 + 2d_1 \sin\alpha_1 \delta l_2\right) \\ \delta\alpha_1 = \frac{1}{|D|^a} \left(-2\sin\alpha_1 \delta l_1 + \frac{A_1}{k_n} \sin\alpha_1 \delta l_2 + \frac{A_1}{k_n} \delta l_2 + 3\cos\alpha_1 \delta l_2\right) \end{cases} \tag{B2}$$

where $|D|^a = \frac{2}{k_n}\left[(B_1 \sin\alpha_1 + A_1 d_1 \cos\alpha_1)(\sin\alpha_1 + 1) - F_2 \sin\alpha_1 + k_n d_1 \cos^2\alpha_1 + 2k_n d_1\right]$

Then, Equation (B2) is substituted into Equation (B1):

$$\frac{1}{|D|^a} \begin{bmatrix} K_{11}^a & K_{12}^a \\ K_{21}^a & K_{22}^a \end{bmatrix} \begin{bmatrix} \delta l_1 \\ \delta l_2 \end{bmatrix} = \begin{bmatrix} \delta F_1^a \\ \delta F_2 \end{bmatrix} \tag{B3}$$

where

$$\begin{cases} K_{11}^a = 2\left(F_2 \sin\alpha_1 - k_n d_1 \cos^2\alpha_1 - k_t d_1 \sin^2\alpha_1\right) \\ K_{12}^a = (k_t d_1 \sin\alpha_1 - F_2)\left(\frac{A_1}{k_n} \sin\alpha_1 + \frac{A_1}{k_n} + 3\cos\alpha_1\right) \\ \qquad - \cos\alpha_1 (B_1 \sin\alpha_1 + B_1 - F_2 + 2k_n d_1 \sin\alpha_1) \\ K_{21}^a = 2(k_t - k_n) d_1 \sin\alpha_1 \cos\alpha_1 - 2F_1^a \sin\alpha_1 \\ K_{22}^a = \left(F_1^a - k_t d_1 \cos\alpha_1\right)\left(\frac{A_1}{k_n} \sin\alpha_1 + \frac{A_1}{k_n} + 3\cos\alpha_1\right) \\ \qquad - \sin\alpha_1 (B_1 \sin\alpha_1 + B_1 - F_2 + 2k_n d_1 \sin\alpha_1) \end{cases} \tag{B4}$$

Similarly, for Hexagon B,

$$\frac{1}{|D|^b} \begin{bmatrix} K_{11}^b & K_{12}^b \\ K_{21}^b & K_{22}^b \end{bmatrix} \begin{bmatrix} \delta l_1 \\ \delta l_3 \end{bmatrix} = \begin{bmatrix} \delta F_1^b \\ \delta F_3 \end{bmatrix} \tag{B5}$$

where

$$\begin{cases} K_{11}^b = 2\left(F_3 \sin\alpha_2 - k_n d_3 \cos^2\alpha_2 - k_t d_3 \sin^2\alpha_2\right) \\ K_{12}^b = (k_t d_3 \sin\alpha_2 - F_3)\left(\frac{A_3}{k_n} \sin\alpha_2 + \frac{A_3}{k_n} + 3\cos\alpha_2\right) \\ \qquad - \cos\alpha_2 (B_3 \sin\alpha_2 + B_3 - F_3 + 2k_n d_3 \sin\alpha_2) \\ K_{21}^b = 2(k_t - k_n) d_3 \sin\alpha_2 \cos\alpha_2 - 2F_1^b \sin\alpha_2 \\ K_{22}^b = \left(F_1^b - k_t d_3 \cos\alpha_2\right)\left(\frac{A_3}{k_n} \sin\alpha_2 + \frac{A_3}{k_n} + 3\cos\alpha_2\right) \\ \qquad - \sin\alpha_2 (B_3 \sin\alpha_2 + B_3 - F_3 + 2k_n d_3 \sin\alpha_2) \end{cases} \tag{B6}$$

with $|D|^b = \frac{2}{k_n}\left[(B_3 \sin\alpha_2 + A_3 d_3 \cos\alpha_2)(\sin\alpha_2 + 1) - F_3 \sin\alpha_2 + k_n d_3 \cos^2\alpha_2 + 2k_n d_3\right]$

Finally, Equation (15) is recovered, with

$$\begin{cases} \delta F_1 = \left(\frac{1}{|D|^a} K_{11}^a + \frac{1}{|D|^b} K_{11}^b\right)\delta l_1 + \frac{1}{|D|^a} K_{12}^a \delta l_2 + \frac{1}{|D|^b} K_{12}^b \delta l_3 \\ \delta F_2 = \frac{1}{|D|^a}\left(K_{21}^a \delta l_1 + K_{22}^a \delta l_2\right) \\ \delta F_3 = \frac{1}{|D|^b}\left(K_{21}^b \delta l_1 + K_{22}^b \delta l_3\right) \end{cases} \tag{B7}$$

ACKNOWLEDGEMENTS

This work is supported by a scholarship from the China Scholarship Council (CSC) under Grant CSC No. 201406250016, the National Natural Science Foundation of China (Grant No. 51579179), and the Region Pays de la Loire of France (project RI-ADAPTCLIM).

REFERENCES

1. Guo N, Zhao JD. 3D multiscale modeling of strain localization in granular media. *Computers and Geotechnics* 2016; **80**:360–372.
2. Chang CS, Yin ZY, Hicher PY. Micromechanical analysis for interparticle and assembly instability of sand. *Journal of Engineering Mechanics* 2010; **137**(3):155–168.
3. Darve F, Servant G, Laouafa F, Khoa HDV. Failure in geomaterials: continuous and discrete analyses. *Computer Methods in Applied Mechanics and Engineering* 2004; **193**(27):3057–3085.
4. Nicot F, Sibille L, Darve F. Bifurcation in granular materials: an attempt for a unified framework. *International Journal of Solids and Structures* 2009; **46**(22):3938–3947.
5. Yin ZY, Huang HW, Hicher PY. Elastoplastic modeling of sand-silt mixtures. *Soils and Foundations* 2016; **56**(3):520–532.
6. Yao YP, Lu DC, Zhou AN, Zou B. Generalized non-linear strength theory and transformed stress space. *Science in China Series E: Technological Sciences* 2004; **47**(6):691–709.
7. Liu HB, Zou DG. Associated generalized plasticity framework for modeling gravelly soils considering particle breakage. *Journal of Engineering Mechanics* 2012; **139**(5):606–615.
8. Chang CS, Yin ZY. Micromechanical modeling for inherent anisotropy in granular materials. *Journal of Engineering Mechanics* 2009; **136**(7):830–839.
9. Yin ZY, Chang CS. Stress–dilatancy behavior for sand under loading and unloading conditions. *International Journal for Numerical and Analytical Methods in Geomechanics* 2013; **37**(8):855–870.
10. Yin ZY, Chang CS, Hicher PY. Micromechanical modelling for effect of inherent anisotropy on cyclic behaviour of sand. *International Journal of Solids and Structures* 2010; **47**(14):1933–1951.
11. Yin ZY, Xu Q, Chang CS. Modeling cyclic behavior of clay by micromechanical approach. *Journal of Engineering Mechanics* 2012; **139**(9):1305–1309.
12. Nicot F, Daouadji A, Laouafa F, Darve F. Second-order work, kinetic energy and diffuse failure in granular materials. *Granular Matter* 2011; **13**(1):19–28.
13. Tordesillas A, Walker DM, Lin Q. Force cycles and force chains. *Physical Review E* 2010; **81**(1):011–302.
14. Zhu H, Nicot F, Darve F. Meso-structure evolution in a 2D granular material during biaxial loading. *Granular Matter* 2016; **18**(1):1–12.
15. Drucker DC, Prager W. Soil mechanics and plastic analysis or limit design. *Quarterly of Applied Mathematics* 1952; **10**(2):157–165.
16. Hill R. On the classical constitutive laws for elastic-plastic solids. In *Recent Progress in Applied Mechanics,* F.K.G. Odqvist Volume, Vol. 241. Wiley: New York, 1967; 241–249.
17. Rice JR. On the structure of stress-strain relations for time-dependent plastic deformation in metals. *Journal of Applied Mechanics* 1970; **37**(3):728–737.
18. Rice JR. Continuum mechanics and thermodynamics of plasticity in relation to microscale deformation mechanisms. In *Constitutive Equations in Plasticity*. Massachusetts Institute of Technology Press: Cambridge, 1975; 23–79.
19. Yao YP, Sun DA, Matsuoka H. A unified constitutive model for both clay and sand with hardening parameter independent on stress path. *Computers and Geotechnics* 2008; **35**(2):210–222.
20. Bažant ZP. Endochronic inelasticity and incremental plasticity. *International Journal of Solids and Structures* 1978; **14**(9):691–714.
21. Kolymbas D. An outline of hypoplasticity. *Archive of Applied Mechanics* 1991; **61**(3):143–151.
22. Darve F. The expression of rheological laws in incremental form and the main classes of constitutive equations. In *Geomaterials Constitutive Equations and Modelling*, Darve F (ed.). Taylor & Francis Books: London, 1990; 123–148.
23. Darve F, Flavigny E, Meghachou M. Yield surfaces and principle of superposition: revisit through incrementally non-linear constitutive relations. *International Journal of Plasticity* 1995; **11**(8):927–948.

24. Fonseca J, Sim WW, Shire T, O'Sullivan C. Microstructural analysis of sands with varying degrees of internal stability. *Géotechnique* 2014; **64**(5):405–411.
25. Kruyt NP, Rothenburg L. Probability density functions of contact forces for cohesionless frictional granular materials. *International Journal of Solids and Structures* 2002; **39**(3):571–583.
26. Cambou B, Dubujet P, Emeriault F, Sidoroff F. Homogenization for granular materials. *European Journal of Mechanics. A. Solids* 1995; **14**(2):255–276.
27. Chang CS, Hicher PY, Yin ZY, Kong LR. Elastoplastic model for clay with microstructural consideration. *Journal of Engineering Mechanics* 2009; **135**(9):917–931.
28. Nicot F, Darve F, Group R. A multi-scale approach to granular materials. *Mechanics of Materials* 2005; **37**(9): 980–1006.
29. Yin ZY, Chang CS, Hicher PY, Karstunen M. Micromechanical analysis of kinematic hardening in natural clay. *International Journal of Plasticity* 2009; **25**(8):1413–1435.
30. Nicot F, Darve F. The H-microdirectional model: accounting for a mesoscopic scale. *Mechanics of Materials* 2011; **43**(12):918–929.
31. Nicot F. Constitutive modelling of a snow cover with a change in scale. *European Journal of Mechanics-A/Solids* 2003; **22**(3):325–340.
32. Cundall PA, Hart RD. Numerical modelling of discontinua. *Engineering Computations* 1992; **9**(2):101–113.
33. Love AEH. *A Treatise on the Mathematical Theory of Elasticity*, Vol. 1. Cambridge University Press: Cambridge, 1927.
34. Christoffersen J, Mehrabadi MM, Nemat-Nasser S. A micromechanical description of granular material behavior. *Journal of Applied Mechanics* 1981; **48**(2):339–344.
35. Mehrabadi MM, Nemat-Nasser S, Oda M. On statistical description of stress and fabric in granular materials. *International Journal for Numerical and Analytical Methods in Geomechanics* 1982; **6**(1):95–108.
36. Kuhn MR, Bagi K. Contact rolling and deformation in granular media. *International Journal of Solids and Structures* 2004; **41**(21):5793–5820.
37. Oda M, Konishi J, Nemat-Nasser S. Experimental micromechanical evaluation of strength of granular materials: effects of particle rolling. *Mechanics of Materials* 1982; **1**(4):269–283.
38. Oda M, Iwashita K, Kakiuchi T. Importance of particle rotation in the mechanics of granular materials. *Powders and Grains* 1997; **97**:207–210.
39. De Saxcé G, Fortin J, Millet O. About the numerical simulation of the dynamics of granular media and the definition of the mean stress tensor. *Mechanics of Materials* 2004; **36**(12):1175–1184.
40. Nicot F, Hadda N, Guessasma M, Fortin J, Millet O. On the definition of the stress tensor in granular media. *International Journal of Solids and Structures* 2013; **50**(14):2508–2517.
41. Valentino R, Barla G, Montrasio L. Experimental analysis and micromechanical modelling of dry granular flow and impacts in laboratory flume tests. *Rock Mechanics and Rock Engineering* 2008; **41**(1):153–177.